Electric-Field Assisted Modulation of Surface Thermochemistry

Manish Shetty[1], M. Alexander Ardagh[1,2], Yutong Pang[1], Omar A. Abdelrahman[2,3], Paul J. Dauenhauer[1,2,*]

[1] Department of Chemical Engineering and Materials Science, University of Minnesota, 421 Washington Ave. SE, Minneapolis, MN 55455, USA

[2] Catalysis Center for Energy Innovation, a U.S. Department of Energy Frontiers Research Center, University of Delaware, 221 Academy Street, Newark, DE, 19716, USA

[3] Department of Chemical Engineering, University of Massachusetts Amherst, 686 N. Pleasant Street, Amherst, MA, 01003, USA

*Corresponding author: hauer@umn.edu

Abstract. Conventional catalyst design has enhanced reactivity and product selectivity through control of surface thermochemistry by tunable surface composition and the surrounding environment (e.g., pore structure). In this work, the prospect for electric field towards controlling product selectivity and reaction networks on the Pt(111) surface was evaluated with periodic density functional theory (DFT) calculations in concert with machine learning (ML) algorithms. Linear scaling relationships (LSRs) for adsorption energies of surface species in electric field were shown to: (i) be distinct as compared to zero-field LSRs across metals, and (ii) linearly correlate with adsorption energies of H* rather than the binding element. The slope of LSRs linearly correlated with the zero-field dipole moment. A random forest ML regression algorithm predicted field-dependent adsorption energies with a mean absolute error (0.12 eV) comparable to DFT. Overall, this study identifies the path forward for electric field-assisted catalysis, specifically towards catalyst poisoning, product selectivity, and control of reaction pathways.

Introduction. Adsorption and related transition state energies govern the promotion and selectivity of chemical reactions in heterogeneous catalysis.[1-4] For important reactions related to energy and chemical synthesis, adsorption energies on transition metal surfaces have been useful predictors of catalytic performance for both thermal and electrochemical systems.[5-7] The surface energies of simple hydrocarbons and oxygenates correlate with the activity and selectivity for many reactions important to energy, materials, and sustainability.[1, 8-9] As such, prediction and control of adsorption energies provides an opportunity towards optimization and control of catalytic systems.

Conventional approaches to improve the capability of heterogeneous catalysts have historically achieved success through the design and optimization of catalyst composition and structure of active sites.[10-12] However, the limit of performance of *static* active sites such as the peak of the Balandin-Sabatier 'volcano' has prompted a new focus on integrating secondary methods of stimulating reactions in concert with catalysis.[13] Static promotion methods involving plasma, electric and magnetic fields, and mechanical stress have emerged as methods to manipulate reaction rates and product selectivity by altering surface adsorption energies and the energy landscape of reactions.[13-15]

In our previous work, we have alternatively suggested that a catalyst oscillating between distinct thermodynamic states with sufficiently high frequency and amplitude should overcome the Balandin-Sabatier maximum associated with static systems.[16-18] For a general gas-phase reaction of A to B, variation of the adsorption energies of general surface species A* and B* *dynamically* alters the catalyst surface coverage with time. Oscillation of the surface adsorption energy manipulates the heat of reaction and activation energy barrier for the

reversible surface reaction of A* to B*, described by a Brønsted-Evans-Polanyi (BEP) relationship.[19] As such, the time-averaged catalytic activity can be enhanced above the Sabatier maximum as the catalytic system switches between rate-limiting steps, as demonstrated by a recent experimental work on the electro-oxidation of formic acid to carbon dioxide and hydrogen.[20] Recently, this *potentiodynamic* operation was utilized for selective enhancement of electrosynthesis of adiponitrile (main precursor to Nylon-66) by ~325% from acrylonitrile compared to *potentiostatic* operation, in favor of competing production of propionitrile[21]

The adsorption energies of adsorbates need to uniquely vary for a *dynamic* system to provide enhanced reactivity under the same dynamic stimuli.[17-18] Materials design approaches that involve the optimization of catalyst composition have not yet been shown *experimentally* to assist with overcoming the Sabatier maximum, as the adsorption energies of key surface intermediates are typically bound to the same periodic linear scaling relationships.[15, 22] Understanding adsorption energy changes under electronic modification is crucial for the development of secondary promotion methods including the selection of external stimuli (e.g., applied voltage or light). Electric fields are known to affect surface chemistry.[19, 23] Intrinsic local electrostatic fields created by promoters and co-adsorbed ions strongly affect adsorption energies and reaction rates in heterogeneous catalytic systems.[24-28] Interfacial and oriented external electric fields significantly affect product selectivity, including enantioselectivity for intramolecular carbene reactions catalyzed by Ru porphyrins and Diels-Alder cycloadditions of cyclopentadiene.[29-30]

External electric fields also significantly affect the chemisorption of molecules on metal surfaces.[26, 31] In these systems, adsorbates, with or without an intrinsic dipole moment in the gas or liquid phase, interact with metal surfaces to exchange charge density to create adsorbate-surface dipoles. The interaction of these dipoles with electric fields can have profound impact on the adsorption and reaction on the catalyst surface.[19, 23, 32-34] Detailed understanding of the fundamental electronic effects and prediction of the adsorbate binding energy changes with electric field is crucial for the development and prediction of these promotional effects towards reactivity and selectivity of catalytic processes. In addition, while the development of universal scaling relationships that capture the periodic trends among metals have received considerable interest,[2-3, 35-37] these scaling relationships under electric fields are not well understood.

Linear scaling methods are limited in their scope and applicability, as new parameters are to be determined for each reaction family.[38] Recent developments in machine learning (ML) have led to the development of algorithms for extracting relationships in multidimensional systems.[39] Specifically, with the availability of large data sets, ML tools have enabled the use of complex mathematical models towards evaluation of complex patterns.[39] With the possibility of compositional and configurational degrees of freedom available for adsorbates to bind to metals, the chemical space for exploration of the adsorption process on metals is large.[40] Density functional theory (DFT) calculations for adsorbate interaction on metals often utilizes multiple iteration steps, with each step requiring single point energy calculations, which is repeated for every adsorption site, and every adsorbate.[41] As such, DFT calculations are computationally expensive, while lower cost ML tools have an important role to play to predict and explore the chemical landscape for adsorption.

In this work, periodic DFT calculations were conducted to evaluate the influence of a uniform electric field on the adsorption energy changes of adsorbates on Pt(111). Pt is a versatile industrial catalyst, used for hydrotreating, hydrogenation of olefins, and cracking of paraffins.[42] The current study was performed on the most thermodynamically stable Pt facet, Pt(111).[42] Surface adsorbates were selected based on their relevance to a broad range of important chemical transformations catalyzed by Pt including ammonia synthesis, methanol decomposition, formaldehyde and formic acid synthesis, and other reforming and

decomposition reactions. In addition, the atomic halides fluorine and chlorine, sulfur, and thiol were considered to extend the understanding beyond oxygenated hydrocarbons. First, the fundamental electronic effects corresponding to the adsorbate-surface interactions under an electric field have been identified, and scaling relationships were developed to correlate field-dependent adsorption and reaction energies. Adsorption energies were then predicted from ML regression algorithms and compared with DFT calculated adsorption energies. These molecular insights then provided insights into chemical reactions including mitigation of catalyst poison and coke formation, tuning of product selectivity, and rate acceleration.

Methods. *Density functional theory (DFT) calculations*. Spin-polarized periodic DFT calculations were performed with MedeA VASP using the ab-initio total-energy and molecular dynamics package VASP 5.4.4 (Vienna ab-initio simulation package) developed at the "Institut fur Materialphysik" of the University at Vienna.[43] The generalized gradient (GGA) corrected Perdew−Burke−Ernzerhof (PBE)[44] exchange correlation functional was used with the projector augmented wave (PAW) method[45] to describe atom cores, and the plane wave basis-set was expanded to a kinetic energy maximum of 400 eV for Kohn-Sham orbitals, in line with previously reported values.[24, 46] The dispersion interactions were modeled using DFT-D3 method with no damping.[47] Conjugate-gradient algorithm was adopted to relax the ions to their ground state. Geometries were considered optimized when electronic energy changes were below 10^{-5} eV, and the ionic forces below 0.02 eV $Å^{-1}$. A Gaussian smearing profile with a smearing parameter of 0.05 eV was imposed at the Fermi level, and energies were extrapolated to zero smearing.

First, bulk fcc Pt was optimized, and the lattice constant was found to be 3.9672 Å, as compared to an experimental value 3.9239 Å[48] (within 1.1% of experimental value). The Pt(111) surface was modeled using a 2 x 2 supercell with four Pt layers and 13.8 Å of vacuum, giving a coverage of ¼ monolayer (Figure S1a), in line with previous studies.[24, 26] The middle two layers of Pt were fixed, and the top and bottom layers were allowed to relax. A 10 x 10 x 10 Monkhorst-Pack k-point mesh was used to sample the Brillouin zone for bulk lattice and 6 x 6 x 1 for the vacuum slab. k-point mesh from 6 x 6 x 1 and 10 x 10 x 1 were tested for the adsorption energy for CO* at the atop site. The energy values were within ~0.1 eV (within the errors of DFT) justifying the choice of k-point mesh of 6 x 6 x 1. The adsorbates were modeled as gas phase molecules in a 15 Å x 15 Å x 15 Å box. Molecules were adsorbed on four types of sites on the (111) surface; atop, fcc and hcp hollow sites, and bridge sites (Figure S1b). Atop sites are named as they are located directly atop a Pt atom, while bridge sites lie at the intersection of two neighboring Pt atoms. Threefold hollow hcp sites are located directly above a subsurface Pt atom while threefold hollow fcc sites lie at the intersection with no Pt atom directly below (Figure S1b).

An external electric field perpendicular to the slab was imposed using the method proposed by Neugebauer and Scheffler.[49] In this method, an electric field was generated without the addition of any external charge and the inclusion of an artificial dipole layer that polarizes the top and bottom layer with opposite charges, and an electric field of opposite sign in the vacuum slab (Figure S1c). A positive field corresponded to depletion of electrons on the adsorbate side of the Pt slab. To determine the effect of the electric field on the binding energy of adsorbates that arrive outside the electric field, the adsorbate energies were calculated without electric fields, and the energies of the bare slab and slab with adsorbates were calculated in the presence of applied electric field,

$$\Delta E_0 = E_{Pt-ads} - E_{Pt-slab} - E_{ads} \quad (1)$$

where $E_{Pt\text{-}ads}$, $E_{Pt\text{-}slab}$ and E_{ads} are the energies for the Pt slab with adsorbed molecules, bare slab, and gas-phase adsorbates, respectively. The adsorption energies were calculated between electric field values of ±1.0 V/ Å for most adsorbates. Electric field strength of 1.0 V/Å has been estimated for an electrode potential of 3 V,[24] proximate cations

inside zeolite cavities.[29] and the vicinity (within ~ 5 Å) of alkali metal ions such as K^+ on metal surfaces.[33]

The change in adsorption energy with varying electric field is governed by the direction and magnitude of metal-adsorbate charge polarization, characterized by a zero-field surface-dipole moment, μ_0. The energy change of adsorption energies on interaction with applied electric field is given by equation 2 below,[31]

$$\Delta E = -\mu_0 F \qquad (2)$$

where μ_0 is the adsorbate dipole moment under zero electric field, and *F* is the value of the external applied electric field. The surface-adsorbate dipole moment changes with applied electric field which introduces a second-order correction to the interaction of the adsorbate with electric field, [31]

$$d\mu = \alpha\, dF \qquad (3)$$

where α is the adsorbate polarizability at the metal surface. The adsorbate polarizability parameter, α, is unique to each adsorbate-surface combination.[31] Taken together, the change in adsorption energy can then be represented as,

$$\Delta E = -\mu_0 F - \frac{1}{2}\alpha F^2 \qquad (4)$$

The calculations performed for CO* at atop and fcc sites on a 4 x 4 supercell (1/16 monolayer) showed similar trends in values of dipole moments, and polarizabilities (Table S1). In order to test the effect of other GGA functionals, CO* adsorption energy, surface-adsorbate dipole moments, and polarizability values were evaluated for the RPBE exchange correlation functional[50] (reported to be more accurate than PBE)[51]. The trends in the adsorption energy, surface-adsorbate dipole moments, and polarizability for CO* at atop and fcc sites were in good agreement with PBE (Table S2). The calculated values of the dipole moments, polarizability, and adsorption energies in this study for O*, H*, C*, N*, NH_3*, NH_2*, NH*, CH_3*, CH_2*, CH*, CO*, NO*, and OH* were in good agreement with Deshlahra et al.[26], and Mavrikakis and coworkers.[42]

Charge density calculations were performed as single point calculations on the optimized zero-field geometry. The charge density difference (ρ_{diff}) was calculated as the difference between the charge density of the vacuum slab with the adsorbate and the charge density of the adsorbate and the slab alone. The isosurfaces of ρ_{diff} were plotted with the aid of VESTA software package.[52]

$$\rho_{diff} = \rho_{Pt-ads} - \rho_{Pt-slab} - \rho_{ads} \qquad (5)$$

The work function of the surface was calculated as the difference between the fermi level and maximum energy in vacuum of the periodic supercell.

Machine learning. Machine learning was conducted using the Explorer application in the Weka v3.8.4 software. The following method was conducted for two versions of the data set: (i) an initial version that omitted physisorbed diatomic adsorbates O_2 and N_2 and (ii) another version with the complete data set. Adsorption energies and all other attributes were normalized to a zero-to-one scale to facilitate algorithm training. Normalization involved rescaling all attributes to zero-to-one without changing the distribution of each attribute (i.e. we did not force the data to take on a normal distribution). The considered attributes were elemental composition of the adsorbate given in the subscripts for the generic adsorbate $C_xH_yO_zN_aCl_bF_cS_d$, coordination number of the adsorption site (one for atop, two for bridge and 3 for fcc and hcp hollow sites), electronegativity of the binding element, valence of the binding adsorbate, charge density per Pt under electric field, and the strength of the electric field. Attributes for the model were selected using the Correlation Attribute Evaluator on the full data set; this method calculated Pearson's correlation between each attribute and the target (normalized adsorption energy here). A cutoff of ± 0.20 was selected to remove insignificant attributes from the model. The charge on Pt and electric field strength were included to capture electric field effects on adsorption energy.

Table 1. Adsorption energy, zero-field adsorption energy, zero-field dipole moment and polarizability for atomic and molecular adsorbates, and surface intermediates on the Pt(111) surface (feasible adsorption sites only).

Adsorbates	Adsorption site	ΔE_0 (eV)	μ_0 (eÅ)	α (eÅ^{2}V^{-2})	Adsorbates	Adsorption site	ΔE_0 (eV)	μ_0 (eÅ)	α (eÅ^{2}V^{-2})
Atomic adsorbates									
C*	Atop	-5.07	0.010	0.100	O*	Atop	-3.31	-0.133	0.060
	Fcc	**-7.25**	**0.004**	**0.022**		**Fcc**	**-4.58**	**-0.014**	**0.015**
	Hcp	-7.09	0.003	0.014		Hcp	-4.15	-0.009	0.0004
H*	Atop	-2.76	0.031	0.017	S*	Atop	-3.19	0.002	0.190
	Fcc	**-2.79**	**0.012**	**0.003**		**Fcc**	**-5.32**	**0.098**	**0.075**
	Hcp	-2.71	0.010	0.005		Hcp	-5.12	0.099	0.088
N*	Bridge	-2.76	0.012	0.005	F*	**Atop**	**-3.21**	**-0.227**	**0.005**
	Atop	-2.58	-0.084	0.081		Fcc	-2.88	-0.120	0.040
	Fcc	**-4.88**	**-0.016**	**0.014**		Hcp	-2.74	-0.164	0.041
	Hcp	-4.60	-0.008	0.022	Cl*	Atop	-2.74	-0.119	0.151
						Fcc	**-2.79**	**0.060**	**0.118**
						hcp	-2.64	0.029	0.145
Molecular adsorbates									
CO*	Atop	-1.89	0.040	0.140	NO*	Atop	-1.13	0.161	0.246
	Fcc	**-1.98**	**-0.133**	**0.083**		**Fcc**	**-2.01**	**-0.056**	**0.111**
	Hcp	-1.97	-0.134	0.101		hcp	-1.85	-0.035	0.128
	Bridge	-1.92	-0.107	0.143					
O_2*	**Atop**	**-0.47**	**-0.064**	**0.159**	N_2*	**Atop**	**-0.32**	**0.068**	**0.171**
	Fcc	0.14	-0.105	0.173		Fcc	-0.11	0.021	0.156
	Hcp	0.19	-0.078	0.140		Hcp	-0.11	0.019	0.138
CO_2*	Atop	-0.26	0.020	0.161	H_2O*	**Atop**	**-0.44**	**0.098**	**0.236**
	Bridge	-0.27	0.025	0.155		Bridge	-0.19	0.038	0.120
NH_3*	Atop	-0.97	0.454	0.191	CH_3OH*	Atop	-0.53	0.200	0.379
HCOOH*	Atop	-0.60	0.257	0.273	CH_2O**	Atop-Atop	-0.71	0.066	0.145
Surface intermediates									
OH*	Atop	-1.57	0.123	0.117	SH*	Atop	-1.03	0.136	0.209
	Fcc	-2.11	0.278	0.118		Fcc	-2.66	0.309	0.139
	Bridge	**-2.43**	**0.188**	**0.082**		Hcp	-2.46	0.291	0.158
						Bridge	**-3.17**	**0.169**	**0.102**
CH*	Atop	-4.11	0.298	0.135	CH_2*	Bridge	-5.04	0.150	0.076
	Fcc	**-6.94**	**0.137**	**0.059**	CH_3*	Atop	-2.26	0.121	0.110
	Hcp	-6.81	0.153	0.072					
NH*	Atop	-1.62	0.254	0.110	NH_2*	Atop	-2.09	0.103	0.176
	Fcc	**-4.19**	**0.214**	**0.004**		**Bridge**	**-2.48**	**0.315**	**0.090**
	Hcp	-3.78	0.253	0.048					
COH*	Atop	-1.97	0.822	0.257	CHOH*	Atop	-3.16	0.597	0.088
	Fcc	-3.84	0.471	0.177		**Bridge**	**-3.44**	**0.392**	**0.171**
	Hcp	**-4.80**	**0.186**	**0.146**	CH_2OH*	Atop	-2.36	0.112	0.239
CH_3O*	**Atop**	**-1.85**	**0.108**	**0.206**	CHO*	**Atop**	**-2.70**	**0.024**	**0.197**
	Bridge	-1.67	0.223	0.188		Fcc	-2.55	0.072	0.105
						hcp	-2.46	0.078	0.108
HCOO**	Atop-atop	-2.59	0.186	0.200	COOH*	Atop	-2.78	-0.133	0.233

Several machine learning regression algorithms were tested and compared using three metrics: (i) correlation coefficient, (ii) mean absolute error (MAE), and (iii) root mean squared error (RMSE), given in Table S3. All algorithm training was conducted using default settings for each algorithm and 10-fold cross validation over the full data set. Algorithms tested include the baseline ZeroR algorithm, Linear Regression, Multilayer Perceptron, SMO regression, lBk which is a k-nearest neighbor algorithm, Decision Stump, Random Forest, Random Tree, and REP Tree. Random Forest had the highest performance in all three metrics with the dataset that omitted O_2 and N_2, this model is discussed further in Supplementary Note 1.

Results and Discussion.

Adsorbate binding energy, favorable binding sites, and influence of electric field. Initial computations studied the nature of adsorbates and binding sites on the formation of surface-adsorbate dipoles, including the adsorption energy, zero-field dipole moments, and polarizability of atomic and

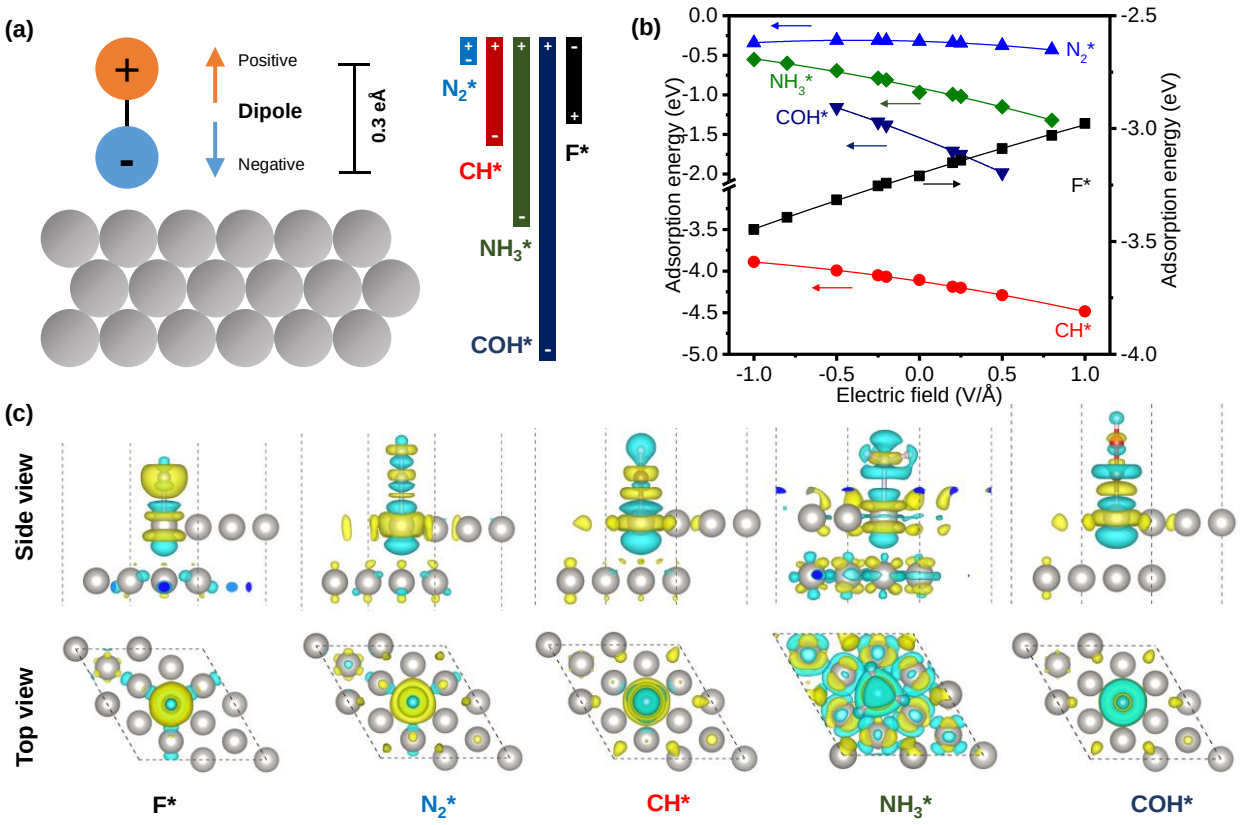

Figure 1. Surface dipoles and charge redistribution on adsorption on the Pt(111) surface. **(a)** Cartoon of the surface dipole on a metal surface, **(b)** variation of adsorption energy with varying electric field for adsorbates F*, CH*, COH*, NH_3* and N_2* on Pt(111) surface, and **(c)** charge density difference of the adsorbates mentioned in (b) in side and top view for the representative adsorbates on Pt(111) surface. The regions corresponding to yellow and blue color correspond to electron enrichment and depletion, respectively.

molecular adsorbates, along with reaction intermediates at the different adsorption sites (Table 1) on Pt(111) surface. For atomic adsorbates, except F*, all adsorbates preferred the fcc hollow site under zero electric field consistent with previous reports,[26, 42] likely due to effective overlap of the 1s for H* and $2p_x$ and $2p_y$ orbitals for the other adsorbates ($3p_x$ and $3p_y$ for adsorbed sulfur, S*) at these higher coordinated sites with metal d_{xz} and d_{yz} orbitals. F* likely requires effective overlap of its $2p_z$ orbital with that of the d_{z2} orbitals at the atop Pt site for a strong sigma overlap. The zero-field dipole moments become more negative with the increased electronegativity of the adsorbate and the lower 2p energy levels from C* to F* that polarizes the surface-adsorbate bond from C* to F*.[53]

All molecular adsorbates, except CO* and NO*, prefer to adsorb at the atop site, consistent with previous reports (CO_2* at atop and bridge sites are nearly isoenergetic).[26, 42, 54-56] Homonuclear adsorbates N_2* and O_2*, as well as CO_2* and H_2O*, exhibit weak binding (physisorption, < 0.3 eV) and low dipole moments. Other molecular adsorbates (NH_3*, CH_3OH*, HCOOH*, and CH_2O**) show higher positive dipole moments and adsorption energies (more negative) due to strong chemisorption and charge transfer from the adsorbates to the metal. In general for surface intermediates, all adsorbates except COOH* exhibit positive dipole moments (Table 1, detailed geometry given in ESI, Figures S10 and S11). The relationship of the adsorbate electronic structure to the adsorption site and observed dipole moment is further described in Supplementary Note 2 (Supporting Information).

While the interaction of surface-adsorbate dipoles with external electric field have been

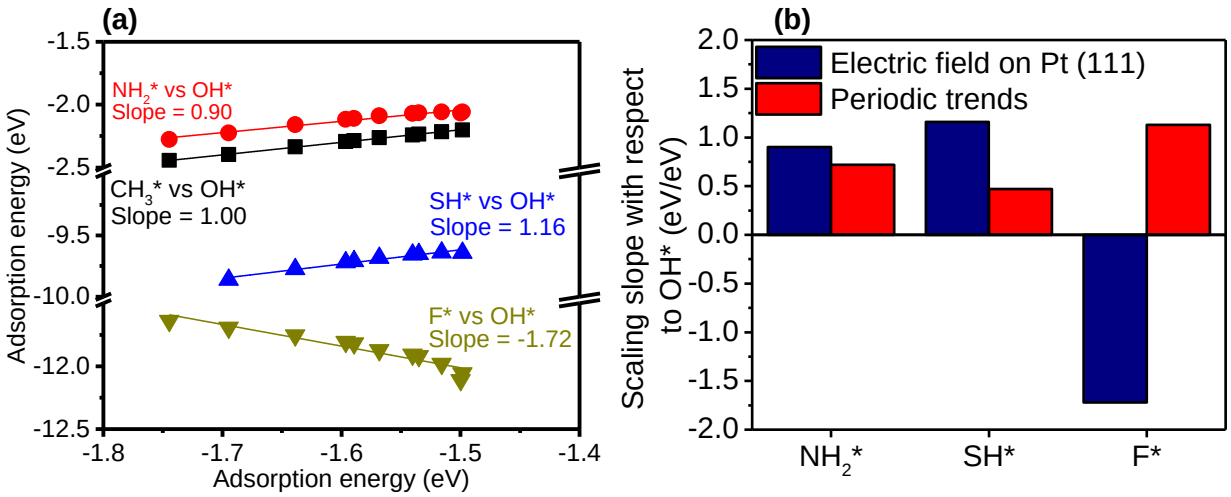

Figure 2. Adsorption energy scaling relationships for monovalent adsorbates on the Pt(111) surface and comparison with periodic scaling relationships. (a) Adsorption scaling relationships for adsorption energy variations under electric field for monovalent surface adsorbates CH_3*, NH_2*, SH* and F* with respect to OH* on atop sites on the Pt(111) surface (R^2 > 0.9), and **(b)** adsorption scaling relationship slopes with electric fields as compared to metals on NH_2*, SH*, and F* with respect to OH*.[2] Adsorption energies of CH_3* and OH* are not expected to correlate on metals. Electric field varied between ± 1.0 V/Å.

studied for individual chemistries,[19, 33, 57] a general understanding of external field influence on adsorption is desired. The interaction of an adsorbate with the Pt(111) surface creates a surface-adsorbate dipole (Figure 1a) on the order of 0.1 to 1.0 eÅ (Table 1). The adsorption energies of a few common atomic/molecular adsorbates and surface intermediates at the atop site for the Pt(111) surface under electric fields were evaluated as shown in Figure 1b.

In general, for all of the considered adsorbates except N_2, the adsorption energy varied by more than ~0.5 eV in the range of varying electric field (±1.0 V/Å). Additionally, all adsorbates except F* exhibited positive dipole moments. The charge density differences in Figure 1c reveal the underlying reasons for the observed dipole moments for the considered adsorbates. For F*, the electron enrichment is concentrated on F, resulting from F being the most electronegative element. For other adsorbates, the electron enrichment instead occurs on the Pt surface (especially for the atop Pt site). The maximum variation is observed for NH_3* and COH*, as expected from equation 4 due to their large dipole moments (Figure 1b and 1c). Overall, it is shown that the adsorption energy of adsorbates can be significantly tuned under strong electric fields.

The adsorption of weakly bound species, and several atomic adsorbates (H*, C*, N*, O*, S* and Cl*) can be enhanced in electric fields by as much as ~0.1 eV. However, as shown by Frisbie and coworkers, electrocatalytic activity towards hydrogen evolution was enhanced by a factor of four with a modulation of H* adsorption energy by only ~0.015 eV on monolayer MoS_2 catalyst, showing immense promise towards rate enhancement by even a small variation of the surface thermochemistry of atomic and weakly bound species.[57] Other molecular adsorbates (NH_3*, CH_3OH*, HCOOH*, CO*, NO* and CH_2O**) have higher positive dipole moments and adsorption energies. Therefore, their adsorption energies can be significantly adjusted as compared to molecules that exhibit weak binding. In addition, the most energetically favorable site can change under electric field due to the different values of zero-field dipole moments and polarizability across the binding sites. For example, CO* at an fcc site has the strongest adsorption at zero field, but the strongest adsorption site changes to the atop site at 1.0 V/Å (Figure S2).

Importantly, surface-adsorbate dipole moments are not correlated to the intrinsic gas-phase dipole moments of the molecules and surface intermediates, as shown in Figure S3. This suggests that the electronic structure of the adsorbates and the interaction with the metal surface is more crucial than the presence of intrinsic dipole moments in the adsorbates. We also note that there are no clear trends in the polarizability, α, of the adsorbates. As such, the gas-phase dipole moments of the adsorbates do not describe the surface-adsorbate dipole moments, and detailed computations are necessary for estimating the surface-adsorbate dipole moments and electric-field dependent adsorption energies.

Linear scaling relationships (LSRs) under electric field. A key factor in catalytic materials design is understanding the variation of adsorbate adsorption energies across metal surfaces and adsorbing atoms.[2-3, 36, 58] LSRs are employed to describe the variations in adsorption energies across adsorbates that bond through a particular atom[2, 36, 58] (e.g. $\Delta E_{ads,CHX*} \sim \Delta E_{ads,C*}$). While these studies help to provide a general framework to understand adsorption through a particular atom and differences in surface binding between different atom types, it is yet to be determined whether such studies can provide similar insights under electric field. The emerging question is the existence of LSRs for adsorption energies on metals in electric fields, and whether these exhibit the same periodic trends of existing scaling relations. To this end, the adsorption energies were calculated for monovalent adsorbates (OH*, CH_3*, NH_2*, SH*, and F*) at atop sites as depicted in Figure 2a. The LSRs effectively describe the adsorption energy changes for these molecules over the range of considered electric field strength ($R^2 > 0.9$). More importantly, these relationships are distinct from periodic trends observed across metals. In particular, the scaling slopes given by $\gamma_{X*/OH*}$ (given in $\Delta E_{ads,X*} = \gamma_{X*/OH*}\Delta E_{ads,OH*}$, where X* is the adsorbate) for NH_2*, SH*, and F* with respect to OH* are 0.72, 0.47, and 1.13, respectively, as compared to 0.90, 1.16, and -1.72 on Pt(111) under electric fields (Figure 2b).[2] Furthermore, these relationships appear to vary for different promotion methods

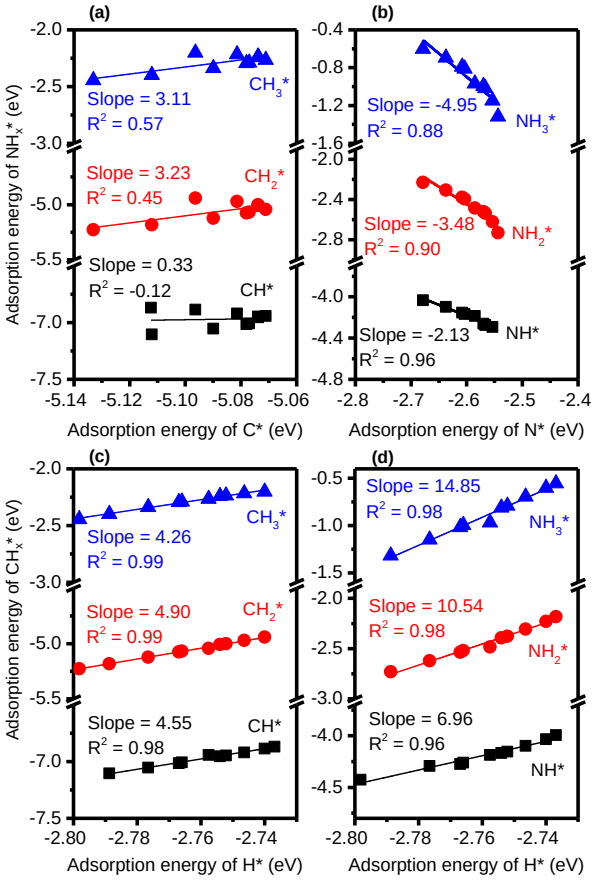

Figure 3. Scaling relationships for adsorption energy variations under electric field for **(a)** NH_x* vs N*, **(b)** NH_x* vs H*, **(c)** CH_x* vs C*, and **(d)** CH_x* vs H* on Pt(111) surface. Electric field varied between ± 1.0 V/Å. NH_3* and CH_3* were at the atop site, CH_2* and NH_2* were at the bridge site, and CH* and NH* were at the fcc site. All the sites are the strongest binding site, as seen in Table 1.

(Figures S8 and S9). For example, $\gamma_{NH3*/NH*}$ ($\Delta E_{ads,NH3*} = \gamma_{NH3*/NH*} * \Delta E_{ads,NH*}$) under electric field on the Pt(111) surface is 1.83 as compared to 0.17 across metals (Figure S8).[17, 59] Taken together, the scaling relationships under electric fields appear to be distinct as compared to periodic trends and change with the promotional methods.

The periodic trends, specifically scaling slopes (γ) for surface intermediates, have been *hitherto* shown with respect to adsorption energies of the binding element (for example, $\Delta E_{ads,CHx*} = \gamma_{CHx*/C*}\Delta E_{ads,C*}$). In varying electric field, the adsorption energies of CH_x* and NH_x* fragments were plotted with respect to the adsorption energies

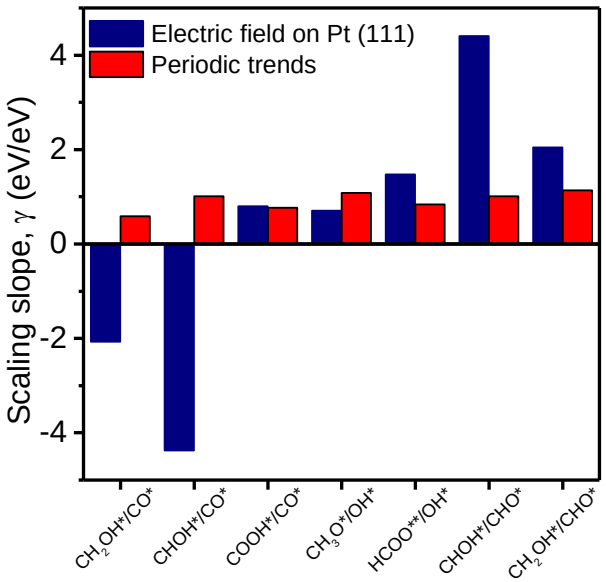

Figure 4. Scaling slopes for CH_xO_y* (CHOH*, CH_2OH*, CH_3O*, and HCOO**) adsorbates with respect to CO* at fcc site, OH* at atop site, and CHO at atop site on the Pt(111) surface under electric field and across metals.[58, 60-61] Electric field varied between ± 1.0 V/Å.

of C* and N* at atop sites (Figure 3a and 3c, respectively). These intermediates do not linearly correlate with adsorption energies of C* or N*, likely due to the large polarizability values of C* and N* at atop sites, leading to stronger second order corrections that weaken the linear correlations in electric field (for example, $\alpha_{C*}/\mu_{0,C*}$ = 10 $ÅV^{-2}$, $\alpha_{N*}/\mu_{0,N*}$ = -1.0 $ÅV^{-2}$). In addition, these slopes are different than the LSRs observed across metals.[17] Specifically, CH_3*, CH_2*, and CH* have slopes ($\gamma_{CHx*/C*}$) of 3.11, 3.23, and 0.33, respectively, with C* under electric field and 0.25, 0.50, and 0.75, respectively, across metals.[58] As H* (atop) shows lower polarizability values as compared to C* and N* at atop sites (0.017 $eÅ^2V^{-2}$ as compared to 0.100 $eÅ^2V^{-2}$, and 0.081 $eÅ^2V^{-2}$, respectively), the CH_x* and NH_x* fragments linearly correlate with the adsorption energy of H* ($\gamma_{CHx*/H*}$ or $\gamma_{NHx*/H*}$) as shown in Figure 3b and 3d. We note that H* adsorption energies at fcc, hcp, and bridge sites linearly correlate with H* adsorption energies at the atop site (Figure S4). Therefore, while the H* at the atop site is considered in Figure 4b and 4d, the linearity of the scaling relationship is independent of the adsorption site of H*.

To further illustrate the differences in the slopes of the LSRs with electric field on the Pt(111) surface and across metals (zero-field), the adsorption energies of CH_xO_y adsorbates (CHOH*, CH_2OH*, CH_3O*, and HCOO**) were correlated with CO* on the fcc site ($\gamma_{CHxOy*/CO*}$), and OH* ($\gamma_{CHxOy*/OH*}$) and CHO* ($\gamma_{CHxOy*/CHO*}$) on atop sites, as shown in Figure 4.[58, 60-61] All adsorbates except $\gamma_{COOH*/CO*}$ show different slopes with electric field as compared to across metals (zero-field). Specifically, both $\gamma_{CHOH*/CO*}$ and $\gamma_{CH2OH*/CO*}$ are negative (-4.37 and -2.07, respectively) with electric field, as compared to positive values (0.59 and 1.01, respectively) across metals. The negative values are a result of the binding properties of CO* on the fcc site of Pt(111). Similar to COOH* (atop), CO* (fcc) also has a negative dipole moment, due to electron back donation to the π^* antibonding orbitals, causing weaker binding on Pt(111) under positive electric field (see Supplementary Note 2 and Figure S2). Additionally, $\gamma_{CH3O*/OH*}$ and $\gamma_{HCOO**/OH*}$ are 0.70 and 1.47 with electric field, and 1.08 and 0.84 across metals. Taken together, the slopes of the LSRs appear to be distinct under electric field on Pt(111) and across metals, as shown earlier for monovalent adsorbates (Figure 3b).

The prospect for LSRs with H* (atop) on the Pt(111) surface was tested for several surface species. Adsorbates common to methane steam reforming corresponding to CH_xO_y* (CH_3OH*, CH_3O*, CH_2O*, CH_2OH*, COH*, CHOH*, and COH*) linearly correlated with the adsorption energy of H*, as shown in Figure 5a ($R^2 > 0.8$). As the magnitude of the scaling slopes with respect to H* are linked to the magnitude of the adsorbate zero-field dipole moment (μ_0), we plotted the scaling slopes ($\gamma_{ads/H*,atop}$) with respect to the corresponding μ_0 for the adsorbates on all sites of Pt(111) (Figure 5b). This shows a strong linear correlation (R^2 ~ 0.99 and normalized mean absolute error, NMAE ~ 0.009). The slope of the scaling relationship is consistent with the simplified derivation between scaling slopes and μ_0 given below, with small second-order corrections from

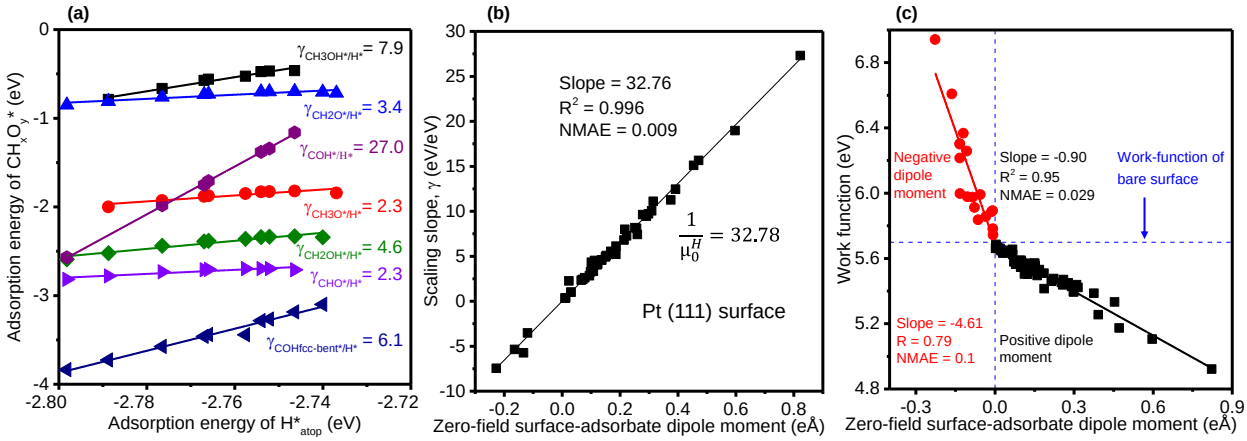

Figure 5. **(a)** Correlation of adsorption energy of CH_xO_y* fragments at Pt atop sites (except $COH_{fcc\text{-}bent}$*) with adsorption energy of H* at atop sites on the Pt(111) surface (R^2 > 0.8). Electric field varied between ± 1.0 eV/Å. **(b)** Scaling relationships for scaling slope referred to Figure 2 with varying zero-field dipole moment (Normalized mean absolute error, NMAE = 0.009). Detailed data provided in Table S4. **(c)** Surface-adsorbate dipole moment with varying work function of the Pt(111) surface with adsorbates under zero electric field (NMAE = 0.029 in the positive dipole moment region and 0.10 in the negative dipole moment region). Detailed data provided in Table S5.

polarizability. The electric-field-dependent adsorption energy variation captured in the slopes $\gamma_{ads/H*,atop}$ (equation 6) follows from the energy variation of individual adsorbates and H* (atop), as given in equation 4,

$$\gamma_{ads/H*atop} = \frac{\Delta E_{ads}}{\Delta E_{H*,atop}} = \frac{-\mu_{0,ads}F - \frac{1}{2}\alpha_{ads}F^2}{-\mu_{0,H*atop}F - \frac{1}{2}\alpha_{H*,atop}F^2} \qquad (6)$$

For external electric fields, the polarizability of H* at the atop site will lead to small corrections (~12% at a maximum electric field of ±1.0 V/Å). Therefore, equation 6 above can be further simplified,

$$\gamma_{ads/H*atop} = \frac{-\mu_{0,ads}F - \frac{1}{2}\alpha_{ads}F^2}{-\mu_{0,H*atop}F} \qquad (7)$$

$$\gamma_{ads/H*atop} = \frac{\mu_{0,ads}}{\mu_{0,H*atop}} + \frac{\alpha_{ads}F}{2} \qquad (8)$$

Figure 5b between γ_{H*atop} and $\mu_{0,ads}$ holds for adsorbates with low polarizability values. This can be rationalized from equation 8 above with the slope of the curve given by $(\mu_{0,H*atop})^{-1}$. This relationship enables the estimation of field-dependent adsorption energy, specifically the first-order correction with the calculation of zero-field dipole moment of the adsorbates. Therefore, for adsorbates with low polarizability on the Pt(111) surface, i.e., sulfur S* (except atop), fluorine F*, and all hydrogenated adsorbates (see Table S4), the computation of $\mu_{0,ads}$ enables the estimation of field-dependent adsorption energies with the aid of figure 5b. We note that the work-function of the surface due to the charge transfer between the adsorbate and the catalyst surface is also linearly correlated with the zero-field dipole moments (Figure 5c) for all adsorbates. Interestingly, the work function variation with surface-adsorbate dipole moments has different slopes of -0.90 ± 0.03 and -4.61 ± 0.57 in the region of positive and negative dipole moments, respectively (details can be found in Supplementary Note 4). Taken together, field-dependent changes on Pt(111) can be estimated with field-independent parameters (μ_0 of adsorbate, and H* at atop site in figure 5b and work-function in figure 5c) of the surface-adsorbate interaction.

To explore the possibility of establishing LSRs across metals with electric field, the zero-field surface-adsorbate dipole moments and polarizability of a few common adsorbates were compared across Pt(111) and Ni(111) surfaces.

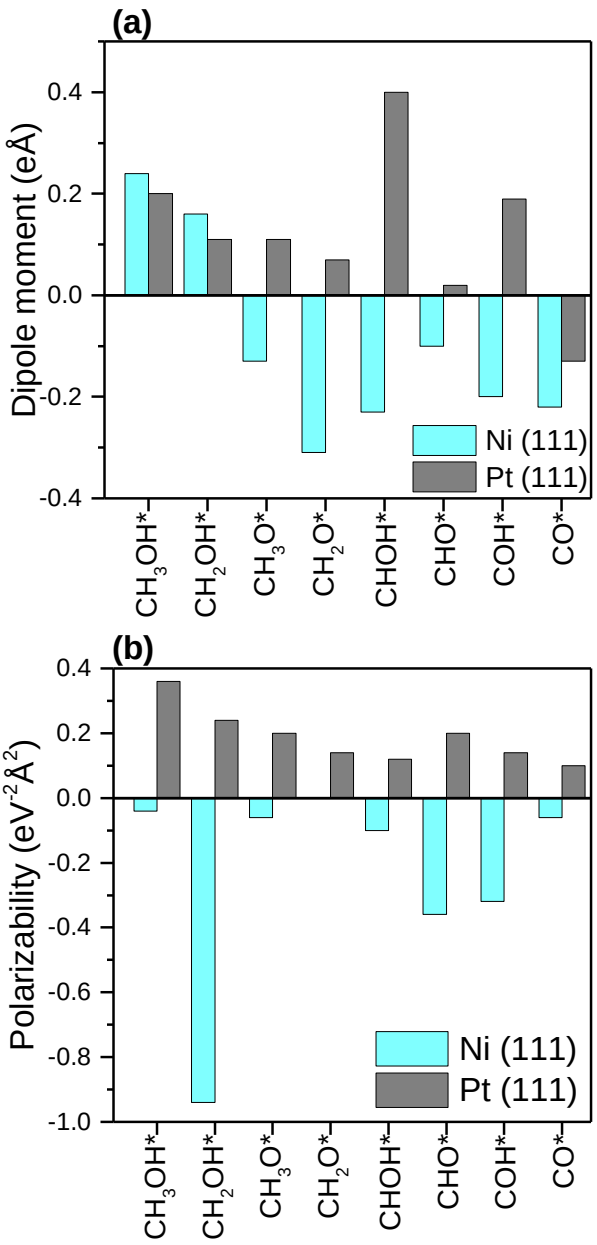

Figure 6. Comparison of surface-adsorbate **(a)** dipole moment and **(b)** polarizability values of common adsorbates on Pt(111) from current work and Ni(111) from McEwen and coworkers.[19, 23]

Importantly, both the values of zero-field surface-adsorbate dipole moments and polarizability vary across metals as shown in Figure 6a and 6b.[19, 23] Further, we evaluated developing LSRs with H* on a Ni(111) surface using data from McEwen and coworkers[19, 46, 62] (details in Supplementary Note 3). Such a relationship with H* (atop) does *not* show a linear correlation (Figure S6 and S7) on the Ni(111) surface due to the large polarizability value of H* on the Ni(111) surface (α_H = 0.062 eÅ^{2}V^{-2} as compared to $\mu_{0,H}$ = 0.01 eÅ). Taken together, the LSRs that exist on Pt(111) surface for zero-field dipole moments and scaling slopes (γ) do not exist on Ni(111) surface. A deeper investigation is required to investigate such relations on individual metals.

Machine learning (ML) of adsorption energy with electric field. The LSR between all adsorbates and H* (atop) in Figure 5b demonstrates the prospect for capturing trends under electric fields across this data set of adsorbates. Moving forward to other metals and adsorbates, a goal will be to construct predictive models that allow us to estimate adsorption energy without expensive DFT calculation. ML is one technique that provides the capability to build predictive models for large datasets with unknown mechanistic connections between input and output variables.[63] There are several examples that demonstrate potential uses and the usefulness of ML in catalysis and material design.[64-65] Random Forest and Neural Network algorithms have shown promise in their ability to predict DFT adsorption energies from first principles and material properties (i.e. crystallinity) from synthesis conditions.[39, 41] In this work, a predictive model was developed for adsorption energy by accounting for adsorbate composition, adsorption geometry, and electric field parameters as input variables in the model.

After evaluating several machine learning algorithms (Table S3), a Random Forest regression algorithm exhibited the highest performance in the prediction of adsorption energies (given below). The Random Forest structure is shown as a scheme in Figure 7A, and our model consisted of 100 decision trees. Each tree included a set of quantitative decisions; an example of these decisions is shown in the Figure 7A inset. Attribute selection was performed to assess attributes with high correlation to adsorption energy and determine which attributes to use in the model; the results are displayed in Figure 7B. The degree of unsaturation (-0.79), coordination number of the binding site (-0.49), and carbon composition (-0.47) were all significantly negatively correlated with adsorption energy. These trends intuitively make sense, because, for example, increased coordination

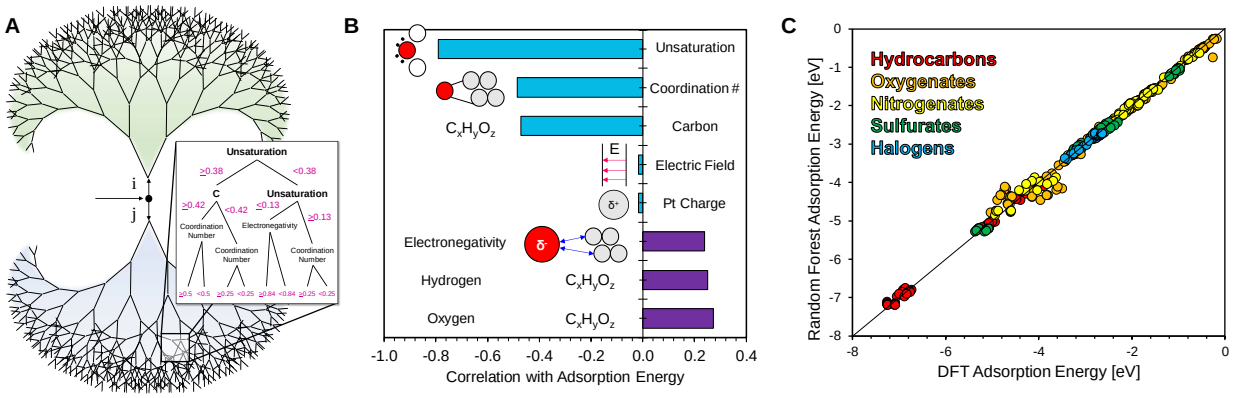

Figure 7. Random Forest regression model for prediction of adsorption energy under electric field on Pt(111). **(A)** Scheme of the Random Forest algorithm, this Random Forest consists of 100 decision trees and one is shown here. An example of some decisions within each tree is shown in the inset. **(B)** Attribute selection for machine learning. The bar values correspond to Pearson's correlation between each attribute and the adsorption energy. **(C)** Parity plot between DFT (x-axis) and Random Forest (y-axis) calculated adsorption energies [eV]. Adsorbates are classified based on their chemical composition as hydrocarbons (red), oxygenates (orange), nitrogenous (yellow), sulfur (green), and halogens (turquoise). The parity line is shown for comparison.

number is expected to lead to greater overlap between adsorbate and metal orbitals which leads to stronger binding (more negative adsorption energies).[24] Finally, DFT and Random Forest calculated adsorption energies were compared to assess the ML model, and a parity plot is depicted in Figure 7C. The correlation coefficient for the Random Forest was 0.99, and the model had an MAE of 0.12 eV and an RMSE of 0.21 eV. The MAE and RMSE are comparable to the typical error (~0.1-0.2 eV) for DFT calculations.[66] The adsorbates were classified based on their chemical composition, and it is apparent from Figure 7C that oxygenated species are most difficult for the model to predict.

Electric-field assisted catalysis. Despite platinum (Pt) being an attractive industrial catalyst, as illustrated in Figure 8, the Pt(111) surface shows weak associative adsorption (physisorption) of some molecular adsorbates, including homonuclear diatomic molecules such as N_2 and O_2 (Figure 8a), and weak activation, as seen from the positive energy for dissociative adsorption of N_2. In contrast, CO and halides (F_2 and Cl_2) are known to poison the catalyst surface (adsorption energy > -1.8 eV).[67-68] For reactions efficiently catalyzed on Pt (for example, HCOOH and NH_3 oxidation),[20] the substrates are chemisorbed (adsorption energy of ~ -0.6 eV for HCOOH, and ~ -1.0 eV for NH_3, see Table 1).

It is desirable for Pt to change its catalytic behavior to resemble other metals. For gas-phase CO_2 hydrogenation on the (111) surface of Pt, Ni, and Ir, the stability of adsorbed HCOO** and CO* varies across these metals (Figure 8b). While HCOO** is energetically favorable to form by ~0.3 eV as compared to CO* on Pt(111) surface, CO* is more favorable to form by ~0.6 eV than HCOO** on the Ni(111) surface. The higher energy of CO* on the Pt(111) surface, is consistent with the high selectivity of CO(g) on Pt.[69] Furthermore, methanation activity on Ni is consistent with the higher stability of CO* on the Ni(111) surface promoting the CO* hydrogenation pathway.[69] On the Ir(111) surface, CO* and HCOO** formation are comparably strong (within ~0.1 eV) and does not show a propensity towards desorption of either CO(g) or HCOOH(g). In addition, for HCOOH(g) decomposition (Figure 8c), while COOH* is energetically stable over HCOO** by ~0.54 eV on Pt(111) surface, HCOO** is more stable than COOH* by ~1 eV on Cu(111) surface. On Ir(111) surface, HCOO** and COOH* are nearly isoenergetic.

The emerging question now arises for how an electric field can be used to modulate stability of surface species, selectivity, and reaction network

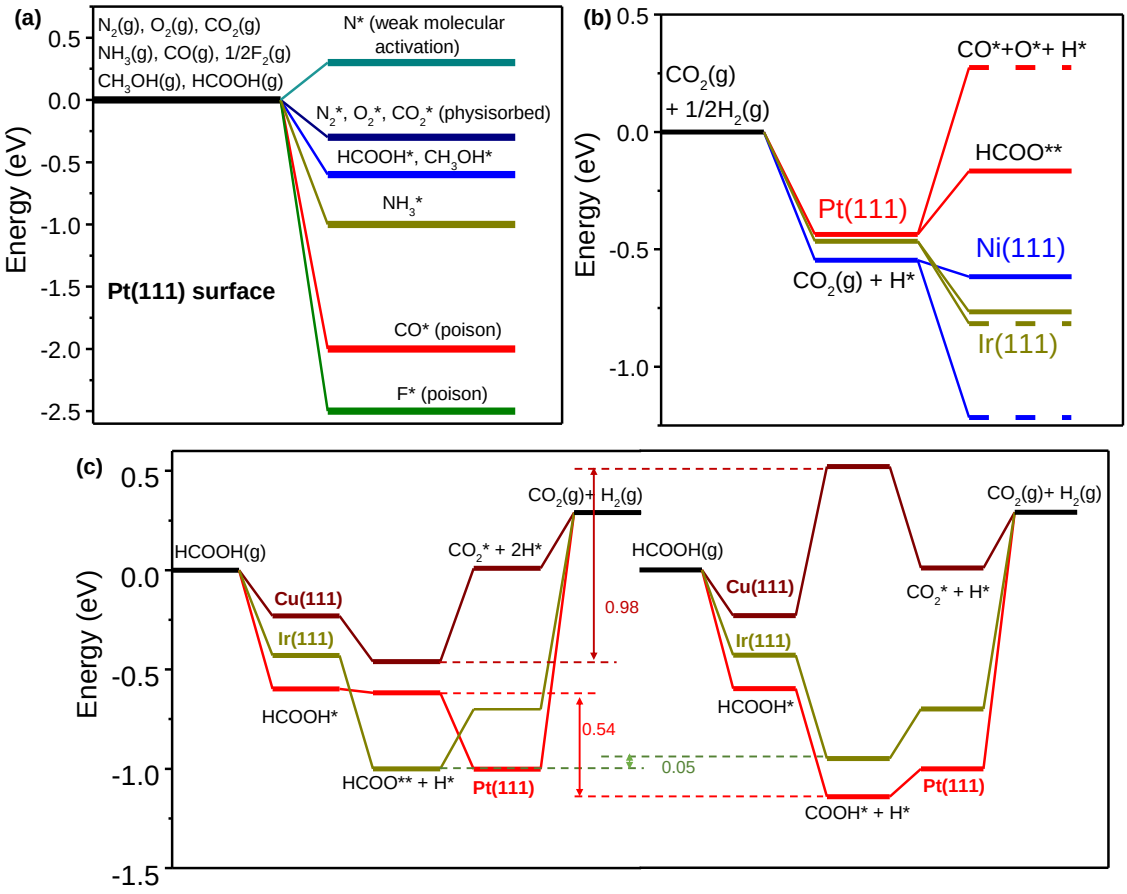

Figure 8. Influence of surface thermochemistry on surface poisoning, reaction networks, and product selectivity. (a) Adsorption energy of molecules that are weakly adsorbed (N_2, O_2, and CO_2), chemisorbed (NH_3, HCOOH, CH_3OH), and poisons (CO and F_2) on the Pt(111) surface. **(b)** Reaction pathway for CO_2 conversion on Pt(111), Ir(111), and Ni(111) surfaces towards CO* and HCOO**. **(c)** Reaction pathway of HCOOH(g) decomposition towards CO_2(g) and H_2(g) on Cu(111), Ir(111), and Pt(111) surfaces. The data in (a) is from current work, while the data in (b) and (c) are based on data from Mavrikakis and coworkers.[70]

that is otherwise typically achieved by changing metals. To this end, we first evaluated the influence of electric field on the adsorption energy of CO* and F* (Figure 9a). The adsorption energy can be reduced by ~0.1 eV and ~0.23 eV for CO* and F*, respectively, at 1.0 V/Å as compared to zero electric field (0.27 and 0.47 eV at 1.0 V/Å compared to -1.0 V/Å, respectively). Therefore, electric field can be employed to partially reduce the coverage of poisons. Next, we considered the formation of coke from the dehydrogenation of CH* intermediate, formed during methane steam reforming (Figure 9b). On application of 1.0 eV/Å electric field, the reaction energy increased to ~0.2 eV compared to ~ -0.1 eV in zero electric field. The reaction activation energies are correlated with the reaction energy changes via the BEP relationship.[3] Therefore, the rates of coke formation will also be reduced on the Pt (111) surface with a positive electric field. Taken together, electric field can potentially be used to enhance catalysts by limiting the adsorption of poisons and mitigating coke formation on the catalyst surface.

As another example, the field-dependent thermochemistry of CO_2 hydrogenation (Figure 9c and d) was investigated next. CO_2 hydrogenation can be considered to follow reverse water-gas-shift, and CO* hydrogenation pathways mediated by the adsorbed CO* and formate (HCOO**) pathway.[69] CO_2* and H* are adsorbed with a total energy of ~0.49 eV. From this state, CO_2* can either undergo C-O bond cleavage to form CO* and O*, or

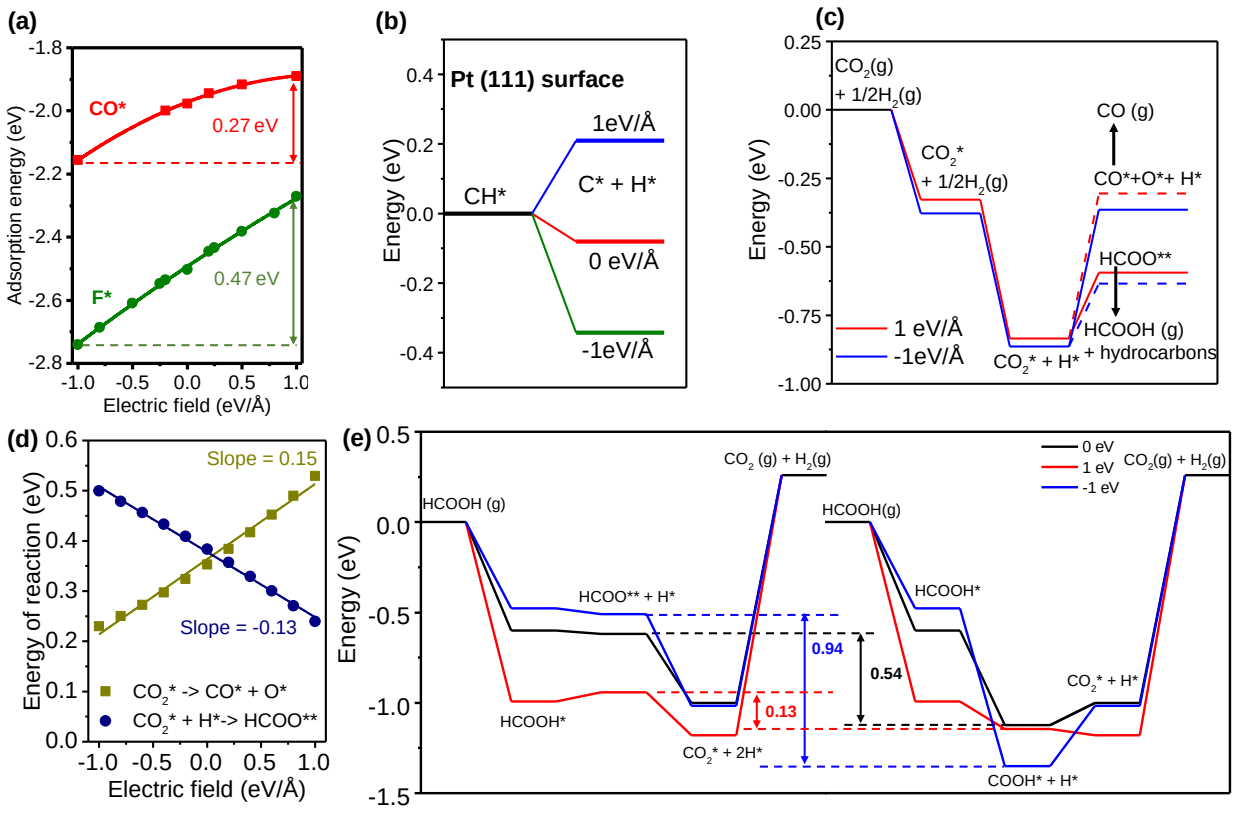

Figure 9. **Electric field influence on reaction networks on the Pt(111) surface. (a)** Adsorption energy of CO* and F* with varying electric field at the site with strongest binding (fcc for CO*, and atop for F*). **(b)** Energy of reaction for coke formation from a CH* fragment in electric field on the Pt(111) surface via C-H dissociation. **(c)** Pathways for gas-phase CO_2 hydrogenation direct C-O cleavage to form CO* and hydrogenation to form HCOO** intermediate. The plot indicates that the product selectivity can be changed by tuning the electric field value between 1.0 and -1.0 V/Å as shown from the lower energy of HCOO** as compared to CO*, O*, and H* at 1.0 eV/Å and the lower energy of CO*, O*, and H* as compared to HCOO** at -1.0 V/Å. **(d)** Linear scaling of the heat of reaction with respect to varying electric field for elementary steps towards CO* and HCOO** formation from CO_2*. The slopes of the correlation under electric field is the sum of dipole moments of products subtracted by the sum of dipole moments of reactants. All energy values provided in eV. **(e)** Pathways for gas-phase formic acid decomposition to CO_2 and H_2 through the HCOO** and COOH* intermediates. The plot shows that the relative stability can be varied by ~0.8 eV between ± 1.0 V/Å.

undergo hydrogenation to form HCOO**. The HCOO** intermediate can be stabilized by ~0.3 eV relative to CO* at 1.0 V/Å, while CO* is stabilized relative to HCOO** by ~0.3 eV at -1.0 V/Å. As the formate pathway can lead to formation of formic acid, methanol, and other hydrocarbons, this pathway can potentially be promoted at 1.0 V/Å. The formation of CO* can be promoted at -1.0 V/Å (similar to zero field), potentially promoting the methanation pathway, or formation of C_{2+} products, as observed on Cu catalyst. This is due to HCOO** and CO* exhibiting opposite strengthening/weakening effects under electric field (μ_0 values of 0.186 eÅ and -0.133 eÅ, respectively). This example shows the prospect for electric field towards modulation of reaction pathways on Pt. In addition, the energy of the elementary reaction of HCOO**, or CO* and O* formation from CO_2* linearly correlates with electric fields, with a slope given by the dipole moment of CO_2* and H* subtracted from the sum of dipole moments of HCOO* or CO*, O* and H*, respectively (0.15 and -0.13). In general, therefore, the field dependent reaction energies and activation energies through BEP relationships can be estimated from the zero-field dipole moments of

reacting species. The field-dependent selectivity and reaction pathways of catalyst surfaces, can be determined, provided they are controlled by the thermodynamic distribution of intermediate, reactant, and product species.

The influence of adsorption energy modulation under electric field can also be potentially used to modulate reaction pathways, as illustrated for HCOOH(g) decomposition to CO_2(g) and H_2(g) on the Pt(111) surface (Figure 9e). Under zero electric field, adsorbed HCOOH* can dehydrogenate to form COOH* or HCOO**, with the COOH* energetically more favorable by ~0.54 eV as compared to HCOO**. While the relative stability of COOH* can be further enhanced to ~0.94 eV at -1.0 eV/Å, the two species (HCOO** and COOH*) become nearly isoenergetic (within 0.13 eV) at 1.0 eV/Å, as seen on the Ir(111) surface with zero field (Figure 8c). With the modulation of the stability of COOH* and HCOO**, factors including the rate limiting step, activation energies of elementary steps, the surface composition of the reaction intermediates, and the reaction rates can change with electric field.

As illustrated in Figure 8 and 9, while changing metals can help to control reaction pathways and tune product selectivity, electric field is a prospective tool to fine-tune adsorption energies on the same catalyst surface that can be otherwise only be achieved through changing the catalyst material or modifying its composition. While the influence of electric fields to enhance molecular activation, reaction rates, product selectivity, and catalyst stability[19] has been demonstrated, this study provides the foundation for evaluation and prediction of electric field effects on Pt for a wide variety of reactions and motivates future study towards evaluation of these effects across metals and alloys.

Conclusions. Periodic DFT calculations were conducted to evaluate the modulation of surface thermochemistry for several common atomic and molecular adsorbates, and surface intermediates relevant for a wide range of organic transformations with electric field on the Pt(111) surface. First, the adsorption energy changes along with the zero-field dipole moment and polarizability of the surface-adsorbate dipoles were computed to estimate the prospect of the modulation of surface thermochemistry of these adsorbates. Linear scaling relationships (LSRs) were developed for adsorbate adsorption energy with respect to adsorption energy of H* at atop sites ($R^2 > 0.9$) with electric field on Pt(111) surface. These E-field LSRs on the Pt(111) surface also varied as compared to zero-field LSRs across metals for the same adsorbates. Specifically, (a) the slopes of the LSRs were distinct with electric field on the Pt(111) surface compared across metals, and (b) the adsorption energies of adsorbates on Pt(111) linearly correlated with H* adsorption energies rather than the adsorption energy of the binding element. The LSRs for scaling slopes ($\gamma_{H^*,atop}$) or work-function with zero-field dipole moment enabled the estimation of field-dependent adsorption energy with the aid of field independent parameters (zero-field dipole moment of adsorbate, and H* at atop site or work-function). Random Forest algorithms predicted the DFT-computed adsorption energies of all adsorbates except N_2 and O_2, within a mean absolute error (MAE) of 0.12 eV. Finally, the prospect for utilizing electric field was also investigated towards desorption of poisons, mitigation of surface coke, and control of product selectivity and reaction networks under electric field on the Pt(111) surface. Overall, this study provides a foundation for future experimental and computational exploration including machine learning approaches for utilizing electric fields for catalysis, specifically towards effective catalyst poisoning, product selectivity, and control of reaction pathways.

Acknowledgements. We acknowledge financial support of the Catalysis Center for Energy Innovation, a U.S. Department of Energy – Energy Frontier Research Center under Grant DE-SC0001004. M.S. is partially supported by the farm families of Minnesota and their corn check-off investment through the Minnesota Corn Growers Association. The authors acknowledge the Minnesota Supercomputing Institute (MSI) at the University of Minnesota for providing resources that contributed to the research results reported within this paper. URL: http://www.msi.umn.edu/. The authors thank Vineet Maliekkal and Professor Turan Birol for their valuable inputs and discussion.

Keywords. Electric field, Adsorption, Catalysis, Methanol, Formic acid, dipole moments, work function

Supporting Information. The detailed geometry, the data and additional discussion referenced in the main text are given in the Electronic Supplementary Information.

Author Contribution. M.S performed the DFT computations. M.A.A. assessed the machine learning algorithms. All authors analyzed the data and contributed to the writing of the manuscript.

References

1. Bligaard, T.; Nørskov, J. K.; Dahl, S.; Matthiesen, J.; Christensen, C. H.; Sehested, J., The Brønsted-Evans-Polanyi relation and the volcano curve in heterogeneous catalysis. *J Catal* **2004,** *224* (1), 206-217.
2. Montemore, M. M.; Medlin, J. W., A Unified Picture of Adsorption on Transition Metals through Different Atoms. *J Am Chem Soc* **2014,** *136* (26), 9272-9275.
3. Nørskov, J. K.; Bligaard, T.; Logadottir, A.; Bahn, S.; Hansen, L. B.; Bollinger, M.; Bengaard, H.; Hammer, B.; Sljivancanin, Z.; Mavrikakis, M.; Xu, Y.; Dahl, S.; Jacobsen, C. J. H., Universality in heterogeneous catalysis. *J Catal* **2002,** *209* (2), 275-278.
4. Dauenhauer, P. J.; Abdelrahman, O. A., A Universal Descriptor for the Entropy of Adsorbed Molecules in Confined Spaces. *ACS Central Science* **2018,** *4* (9), 1235-1243.
5. Medford, A. J.; Vojvodic, A.; Hummelshoj, J. S.; Voss, J.; Abild-Pedersen, F.; Studt, F.; Bligaard, T.; Nilsson, A.; Nørskov, J. K., From the Sabatier principle to a predictive theory of transition-metal heterogeneous catalysis. *J Catal* **2015,** *328*, 36-42.
6. Ulissi, Z. W.; Medford, A. J.; Bligaard, T.; Nørskov, J. K., To address surface reaction network complexity using scaling relations machine learning and DFT calculations. *Nat Commun* **2017,** *8*.
7. Greeley, J.; Jaramillo, T. F.; Bonde, J.; Chorkendorff, I. B.; Nørskov, J. K., Computational high-throughput screening of electrocatalytic materials for hydrogen evolution. *Nat Mater* **2006,** *5* (11), 909-913.
8. Studt, F.; Abild-Pedersen, F.; Varley, J. B.; Nørskov, J. K., CO and CO_2 Hydrogenation to Methanol Calculated Using the BEEF-vdW Functional. *Catal Lett* **2013,** *143* (1), 71-73.
9. Medford, A. J.; Lausche, A. C.; Abild-Pedersen, F.; Temel, B.; Schjodt, N. C.; Nørskov, J. K.; Studt, F., Activity and Selectivity Trends in Synthesis Gas Conversion to Higher Alcohols. *Top Catal* **2014,** *57* (1-4), 135-142.
10. Greeley, J.; Stephens, I. E. L.; Bondarenko, A. S.; Johansson, T. P.; Hansen, H. A.; Jaramillo, T. F.; Rossmeisl, J.; Chorkendorff, I.; Nørskov, J. K., Alloys of platinum and early transition metals as oxygen reduction electrocatalysts. *Nat Chem* **2009,** *1* (7), 552-556.
11. Stamenkovic, V.; Mun, B. S.; Mayrhofer, K. J. J.; Ross, P. N.; Markovic, N. M.; Rossmeisl, J.; Greeley, J.; Nørskov, J. K., Changing the activity of electrocatalysts for oxygen reduction by tuning the surface electronic structure. *Angew Chem Int Edit* **2006,** *45* (18), 2897-2901.
12. Ding, S. P.; Hülsey, M. J.; Perez-Ramirez, J.; Yang, N., Transforming Energy with Single-Atom Catalysts. *Joule* **2019,** *3* (12), 2897-2929.
13. Perez-Ramirez, J.; Lopez, N., Strategies to break linear scaling relationships. *Nat Catal* **2019,** *2* (11), 971-976.
14. Hong, J. M.; Prawer, S.; Murphy, A. B., Plasma Catalysis as an Alternative Route for Ammonia Production: Status, Mechanisms, and Prospects for Progress. *ACS Sustainable Chem Eng* **2018,** *6* (1), 15-31.
15. Hülsey, M. J.; Lim, C. W.; Yan, N., Promoting heterogeneous catalysis beyond catalyst design. *Chem Science* **2020,** *11* (6), 1456-1468.
16. Ardagh, M. A.; Abdelrahman, O. A.; Dauenhauer, P. J., Principles of Dynamic Heterogeneous Catalysis: Surface Resonance and Turnover Frequency Response. *ACS Catal* **2019,** *9* (8), 6929-6937.
17. Ardagh, M. A.; Birol, T.; Zhang, Q.; Abdelrahman, O. A.; Dauenhauer, P. J., Catalytic resonance theory: superVolcanoes, catalytic molecular pumps, and oscillatory steady state. *Catal Sci Technol* **2019,** *9* (18), 5058-5076.

18. Ardagh, M. A.; Shetty, M.; Kuznetsov, A.; Zhang, Q.; Christopher, P.; Vlachos, D. G.; Abdelrahman, O. A.; Dauenhauer, P. J., Catalytic resonance theory: parallel reaction pathway control. *Chem Science* **2020**, *11 (13)*, 3501-3510.
19. Che, F. L.; Gray, J. T.; Ha, S.; McEwen, J. S., Improving Ni Catalysts Using Electric Fields: A DFT and Experimental Study of the Methane Steam Reforming Reaction. *ACS Catal* **2017,** *7* (1), 551-562.
20. Joshua, G.; Matthew, A.; Manish, S.; Sean, B.; Paul, D.; Omar, A., Resonance-Promoted Formic Acid Oxidation via Dynamic Electrocatalytic Modulation. 2020, *ChemRxiv*, doi.org/10.26434/chemrxiv.11972031.v1
21. Blanco, D. E.; Lee, B.; Modestino, M. A., Optimizing organic electrosynthesis through controlled voltage dosing and artificial intelligence. *P Natl Acad Sci USA* **2019,** *116* (36), 17683-17689.
22. Seh, Z. W.; Kibsgaard, J.; Dickens, C. F.; Chorkendorff, I. B.; Norskov, J. K.; Jaramillo, T. F., Combining theory and experiment in electrocatalysis: Insights into materials design. *Science* **2017,** *355* (6321).
23. Che, F. L.; Hensley, A. J.; Ha, S.; McEwen, J. S., Decomposition of methyl species on a Ni(211) surface: investigations of the electric field influence. *Catal Sci Technol* **2014,** *4* (11), 4020-4035.
24. Deshlahra, P.; Wolf, E. E.; Schneider, W. F., A Periodic Density Functional Theory Analysis of CO Chemisorption on Pt(111) in the Presence of Uniform Electric Fields. *J Phys Chem A* **2009,** *113* (16), 4125-4133.
25. Deshlahra, P.; Schneider, W. F.; Bernstein, G. H.; Wolf, E. E., Direct Control of Electron Transfer to the Surface-CO Bond on a Pt/TiO_2 Catalytic Diode. *J Am Chem Soc* **2011,** *133* (41), 16459-16467.
26. Deshlahra, P.; Conway, J.; Wolf, E. E.; Schneider, W. F., Influence of Dipole-Dipole Interactions on Coverage-Dependent Adsorption: CO and NO on Pt(111). *Langmuir* **2012,** *28* (22), 8408-8417.
27. Neophytides, S. G.; Vayenas, C. G., The Effect of Catalyst-Electrode Potential and Work Function on the Chemisorptive Bond of Oxygen on Pt Interfaced with YSZ. *Ionics* **1995,** *1* (1), 80-84.
28. Linic, S.; Barteau, M. A., On the mechanism of Cs promotion in ethylene epoxidation on Ag. *J Am Chem Soc* **2004,** *126* (26), 8086-8087.
29. Gorin, C. F.; Beh, E. S.; Bui, Q. M.; Dick, G. R.; Kanan, M. W., Interfacial Electric Field Effects on a Carbene Reaction Catalyzed by Rh Porphyrins. *J Am Chem Soc* **2013,** *135* (30), 11257-11265.
30. Wang, Z. F.; Danovich, D.; Ramanan, R.; Shaik, S., Oriented-External Electric Fields Create Absolute Enantioselectivity in Diels-Alder Reactions: Importance of the Molecular Dipole Moment. *J Am Chem Soc* **2018,** *140* (41), 13350-13359.
31. Wasileski, S. A.; Koper, M. T. M.; Weaver, M. J., Field-dependent electrode-chemisorbate bonding: Sensitivity of vibrational stark effect and binding energetics to nature of surface coordination. *J Am Chem Soc* **2002,** *124* (11), 2796-2805.
32. Williams, R. D.; Sikdar, S. K., Hydrogenation of Ethylene over Zinc-Oxide Effect of an Electrodynamic Field. *J Catal* **1975,** *38* (1-3), 147-152.
33. Chen, L. D.; Urushihara, M.; Chan, K. R.; Nørskov, J. K., Electric Field Effects in Electrochemical CO_2 Reduction. *ACS Catal* **2016,** *6* (10), 7133-7139.
34. Pacchioni, G.; Lomas, J. R.; Illas, F., Electric field effects in heterogeneous catalysis. *J Mol Catal A* **1997,** *119* (1-3), 263-273.
35. Montemore, M. M.; Medlin, J. W., Site-Specific Scaling Relations for Hydrocarbon Adsorption on Hexagonal Transition Metal Surfaces. *J Phys Chem C* **2013,** *117* (39), 20078-20088.
36. Montemore, M. M.; Medlin, J. W., Predicting and Comparing C-M and O-M Bond Strengths for Adsorption on Transition Metal Surfaces. *J Phys Chem C* **2014,** *118* (5), 2666-2672.
37. Medlin, J. W.; Montemore, M. M., Heterogeneous Catalysis: Scaling the rough heights. *Nat Chem* **2015,** *7* (5), 378-380.
38. Grambow, C. A.; Pattanaik, L.; Green, W. H., Deep Learning of Activation Energies. *J Phys Chem Lett* **2020**, *11*, 2992-2997.
39. Jensen, Z.; Kim, E.; Kwon, S.; Gani, T. Z. H.; Roman-Leshkov, Y.; Moliner, M.; Corma, A.; Olivetti, E., A Machine Learning Approach to Zeolite Synthesis Enabled by Automatic Literature Data Extraction. *ACS Central Science* **2019,** *5* (5), 892-899.

40. Pilania, G.; Wang, C. C.; Jiang, X.; Rajasekaran, S.; Ramprasad, R., Accelerating materials property predictions using machine learning. *Sci Rep-Uk* **2013,** *3*.
41. Ulissi, Z. W.; Tang, M. T.; Xiao, J. P.; Liu, X. Y.; Torelli, D. A.; Karamad, M.; Cummins, K.; Hahn, C.; Lewis, N. S.; Jaramillo, T. F.; Chan, K. R.; Nørskov, J. K., Machine-Learning Methods Enable Exhaustive Searches for Active Bimetallic Facets and Reveal Active Site Motifs for CO_2 Reduction. *ACS Catal* **2017,** *7* (10), 6600-6608.
42. Ford, D. C.; Xu, Y.; Mavrikakis, M., Atomic and molecular adsorption on Pt(111). *Surf Sci* **2005,** *587* (3), 159-174.
43. Kresse, G.; Furthmuller, J., Efficient iterative schemes for ab initio total-energy calculations using a plane-wave basis set. *Phys Rev B* **1996,** *54* (16), 11169-11186.
44. Perdew, J. P.; Burke, K.; Ernzerhof, M., Generalized gradient approximation made simple. *Phys Rev Lett* **1996,** *77* (18), 3865-3868.
45. Kresse, G.; Joubert, D., From ultrasoft pseudopotentials to the projector augmented-wave method. *Phys Rev B* **1999,** *59* (3), 1758-1775.
46. Che, F. L.; Zhang, R. Q.; Hensley, A. J.; Ha, S.; McEwen, J. S., Density functional theory studies of methyl dissociation on a Ni(111) surface in the presence of an external electric field. *Phys Chem Chem Phys* **2014,** *16* (6), 2399-2410.
47. Grimme, S.; Antony, J.; Ehrlich, S.; Krieg, H., A consistent and accurate ab initio parametrization of density functional dispersion correction (DFT-D) for the 94 elements H-Pu. *J Chem Phys* **2010,** *132* (15).
48. Feibelman, P. J.; Hammer, B.; Norskov, J. K.; Wagner, F.; Scheffler, M.; Stumpf, R.; Watwe, R.; Dumesic, J., The CO/Pt(111) puzzle. *J Phys Chem B* **2001,** *105* (18), 4018-4025.
49. Neugebauer, J.; Scheffler, M., Adsorbate-Substrate and Adsorbate-Adsorbate Interactions of Na and K Adlayers on Al(111). *Phys Rev B* **1992,** *46* (24), 16067-16080.
50. Hammer, B.; Hansen, L. B.; Nørskov, J. K., Improved adsorption energetics within density-functional theory using revised Perdew-Burke-Ernzerhof functionals. *Phys Rev B* **1999,** *59* (11), 7413-7421.
51. Wellendorff, J.; Silbaugh, T. L.; Garcia-Pintos, D.; Nørskov, J. K.; Bligaard, T.; Studt, F.; Campbell, C. T., A benchmark database for adsorption bond energies to transition metal surfaces and comparison to selected DFT functionals. *Surf Sci* **2015,** *640*, 36-44.
52. Momma, K.; Izumi, F., VESTA: a three-dimensional visualization system for electronic and structural analysis. *J Appl Crystallogr* **2008,** *41*, 653-658.
53. Roman, T.; Gross, A., Periodic Density-Functional Calculations on Work-Function Change Induced by Adsorption of Halogens on Cu(111). *Phys Rev Lett* **2013,** *110* (15).
54. Matsumoto, M.; Tatsumi, N.; Fukutani, K.; Okano, T., Dynamical low-energy electron diffraction analysis of the structure of nitric oxide on Pt(111). *Surf Sci* **2002,** *513* (3), 485-500.
55. Gland, J. L.; Sexton, B. A.; Fisher, G. B., Oxygen Interactions with the Pt(111) Surface. *Surf Sci* **1980,** *95* (2-3), 587-602.
56. Ray, N. K.; Anderson, A. B., Molecular-Orbital Study of Co Chemisorption on a Pt(111) Surface in the Presence of Potassium. *Surf Sci* **1983,** *125* (3), 803-812.
57. Wang, Y.; Udyavara, S.; Neurock, M.; Frisbie, C. D., Field Effect Modulation of Electrocatalytic Hydrogen Evolution at Back-Gated Two-Dimensional MoS2 Electrodes. *Nano Lett* **2019,** *19* (9), 6118-6123.
58. Montemore, M. M.; Medlin, J. W., Scaling relations between adsorption energies for computational screening and design of catalysts. *Catal Sci Technol* **2014,** *4* (11), 3748-3761.
59. Liu, F. Z.; Xue, T. T.; Wu, C.; Yang, S. C., Coadsorption of CO and O over strained metal surfaces. *Chem Phys Lett* **2019,** *722*, 18-25.
60. Ferrin, P.; Nilekar, A. U.; Greeley, J.; Mavrikakis, M.; Rossmeisl, J., Reactivity descriptors for direct methanol fuel cell anode catalysts. *Surf Sci* **2008,** *602* (21), 3424-3431.
61. Ferrin, P.; Mavrikakis, M., Structure Sensitivity of Methanol Electrooxidation on Transition Metals. *J Am Chem Soc* **2009,** *131* (40), 14381-14389.
62. Che, F. L.; Ha, S.; McEwen, J. S., Elucidating the Role of the Electric Field at the Ni/YSZ Electrode: A DFT Study. *J Phys Chem C* **2016,** *120* (27), 14608-14620.
63. Coley, C. W.; Rogers, L.; Green, W. H.; Jensen, K. F., Computer-Assisted Retrosynthesis Based

on Molecular Similarity. *Acs Central Science* **2017,** *3* (12), 1237-1245.
64. Li, Z.; Ma, X. F.; Xin, H. L., Feature engineering of machine-learning chemisorption models for catalyst design. *Catal Today* **2017,** *280*, 232-238.
65. Raccuglia, P.; Elbert, K. C.; Adler, P. D. F.; Falk, C.; Wenny, M. B.; Mollo, A.; Zeller, M.; Friedler, S. A.; Schrier, J.; Norquist, A. J., Machine-learning-assisted materials discovery using failed experiments. *Nature* **2016,** *533* (7601), 73-76.
66. Gautier, S.; Steinmann, S. N.; Michel, C.; Fleurat-Lessard, P.; Sautet, P., Molecular adsorption at Pt(111). How accurate are DFT functionals? *Phys Chem Chem Phys* **2015,** *17* (43), 28921-28930.
67. Arruda, T. M.; Shyam, B.; Ziegelbauer, J. M.; Mukerjee, S.; Ramaker, D. E., Investigation into the Competitive and Site-Specific Nature of Anion Adsorption on Pt Using In Situ X-ray Absorption Spectroscopy. *J Phys Chem C* **2008,** *112* (46), 18087-18097.
68. Chung, D. Y.; Kim, H. I.; Chung, Y. H.; Lee, M. J.; Yoo, S. J.; Bokare, A. D.; Choi, W.; Sung, Y. E., Inhibition of CO poisoning on Pt catalyst coupled with the reduction of toxic hexavalent chromium in a dual-functional fuel cell. *Sci Rep-Uk* **2014,** *4*.
69. Kattel, S.; Liu, P.; Chen, J. G. G., Tuning Selectivity of CO_2 Hydrogenation Reactions at the Metal/Oxide Interface. *J Am Chem Soc* **2017,** *139* (29), 9739-9754.
70. Herron, J. A.; Scaranto, J.; Ferrin, P.; Li, S.; Mavrikakis, M., Trends in Formic Acid Decomposition on Model Transition Metal Surfaces: A Density Functional Theory study. *ACS Catal* **2014,** *4* (12), 4434-4445.